RSC Advances

PAPER

Cite this: *RSC Adv.*, 2025, **15**, 8657

Surface catalytic effect of Ag nanoparticles and influence of dissolved oxygen on photocatalytic reduction of nitrate†

Bin Huang,[ab] Wei Liu,[bc] Kun Chao,[bd] Dongran Wang,[be] Pengxiang Wang,[be] Tengfeng Xie,[f] Fangming Han,[*be] Yan Mi,[*a] Haibin Tang[*be] and Guowen Meng[be]

Received 3rd February 2025
Accepted 4th March 2025

DOI: 10.1039/d5ra00782h

rsc.li/rsc-advances

Photocatalytic reduction of nitrate is a promising green strategy to remove nitrogen pollutants from water bodies. However, it is a considerable challenge to directly reduce nitrate using photogenerated electrons. In this work, a g-C_3N_4/Ag-nanoparticle composite demonstrating high catalytic activity toward nitrate is constructed using an *in situ* photodeposition method. Based on photoelectrochemical, ion chromatography and nuclear magnetic resonance characterization, Ag nanoparticles were found to exhibit strong surface catalytic activity for reducing NO_3^- to NO_2^-, while g-C_3N_4/Au-nanoparticles exhibited no photocatalytic reduction activity toward NO_3^-. Additionally, the effects of dissolved oxygen on the photocatalysis system of nitrate reduction are analyzed for the first time.

1. Introduction

The massive use of nitrogenous fertilizers in agricultural production and the rapid development of the nitrogen industry have resulted in serious nitrate (NO_3^-) contamination of underground water and natural water bodies.[1–3] NO_3^- can be converted into toxic nitrosamines when ingested by the body, which can induce cellular cancer, malformations and embryotoxicity.[4–7] Thus, removal of NO_3^- from water is critical for ensuring environment safety and human health. Compared with traditional methods such as adsorption,[8,9] ion exchange,[10,11] electrodialysis,[12–14] and biological denitrification,[15,16] photocatalytic reduction of NO_3^- to N_2 gas is a promising technology.[17,18] However, NO_3^- is chemically stable because of the N=O and two N–O bonds with bond energies of 607 and 230 kJ mol^{-1}, respectively. The reduction potential is extremely high for typical semiconductor photocatalysts; *e.g.*, for the first reaction of $NO_3^-/{}^{\bullet}NO_3^{2-}$, it is −0.89 V (*vs.* standard hydrogen electrode, SHE). Moreover, most reported photocatalytic systems are TiO_2-based photocatalysts requiring various hole sacrificial agents, especially formic acid, which results in high production of ${}^{\bullet}CO_2^-$ radicals after oxidation by photogenerated holes and has strong reducibility toward nitrate ($E(CO_2^-/{}^{\bullet}CO_2^-) = -1.81$ V *vs.* SHE) and high selectivity for N_2.[19–23] To replace reducing additives for potential application, high conduction band semiconductors with a higher driving force of photogenerated electrons have been studied to reduce NO_3^-. For example, ZnS,[24] $LiNbO_3$,[25] Pd/$GdCrO_3$,[26] and ZnSe/$BiVO_4$ (ref. 27) showed photocatalytic efficiency and considerable N_2 selectivity with added sacrificial agents. However, they all require strong UV light illumination owing to their wide bandgaps. Moreover, UV light can be strongly absorbed by NO_3^- and NO_2^-, which will be excited to excitation states, thus facilitating their reduction.[28]

Development of photocatalysts with a narrow bandgap, *i.e.* improving the utilization of visible light, is a developing research direction for promoting practical application.[29,30] At present, only few materials, such as oxygen vacancy-enriched P25 decorated with Ag/Cu nanoparticles[31] and graphitic carbon nitride (g-C_3N_4) decorated with Ag nanoparticles,[32] have been reported to exhibit photocatalytic reduction of nitrate performance under visible light, although the selectivity for N_2 is low with NO_2^- as the primary product. Furthermore, revealing their working mechanisms is of great significance for the future design of visible light-sensitive photocatalysts. However, the mechanism is not clear to date. Additionally, all

[a]*Guangxi Key Laboratory of Chemistry and Engineering of Forest Products, Guangxi Minzu University, Nanning, 530006, P. R. China. E-mail: miyan@gxmzu.edu.cn*

[b]*Key Laboratory of Materials Physics, Anhui Key Laboratory of Nanomaterials and Nanotechnology, Institute of Solid State Physics, HFIPS, Chinese Academy of Sciences, 350 Shushanhu Road, Hefei, Anhui 230031, P. R. China. E-mail: hbtang@issp.ac.cn; fmhan@issp.ac.cn*

[c]*Institutes of Physical Science and Information Technology, School of Materials Science and Engineering, Anhui University, Hefei 230601, P. R. China*

[d]*School of Advanced Materials and Nanotechnology, Xidian University, Xi'an, 710126, P. R. China*

[e]*University of Science and Technology of China, 96 Jinzhai Road, Hefei, Anhui 230026, P. R. China*

[f]*Institute of Physical Chemistry, College of Chemistry, Jilin University, Changchun 130012, P. R. China*

† Electronic supplementary information (ESI) available. See DOI: https://doi.org/10.1039/d5ra00782h

previously reported experimental systems worked in an aqueous solution in the absence of dissolved O_2. However, for practical application, the presence of dissolved O_2 in natural water bodies cannot be neglected. Nevertheless, the effects of dissolved O_2 on the photocatalytic reduction of nitrate have not been studied.

Herein, we prepared composite photocatalysts of g-C_3N_4 decorated with Ag nanoparticles (Ag-NPs) and Au-NPs (denoted as CNAg and CNAu, respectively). The surface catalysis activity of Ag-NPs was found to be the dominant mechanism for efficient photocatalytic reduction of nitrate. Moreover, the negative influence of dissolved O_2 in inhibiting nitrate reduction and positive influence in improving oxidation capacity were revealed, providing further guidance for practical applications.

2. Experimental details

2.1 Materials

Urea, silver nitrate, methanol, anhydrous ethanol were purchased from Sinopharm Group Chemical Reagent Co., Ltd. All reagents were of analytical grade and used without further purification. Deionized water (18.2 MΩ) used in all experiments was produced using a Millipore Direct-Q system.

2.2 Synthesis of g-C_3N_4 and g-C_3N_4 decorated with Ag, Au, and Pt nanoparticles

2.2.1 g-C_3N_4 preparation. Graphite phase carbon nitride was prepared by placing 10 g of ground urea in a ceramic crucible, followed by heating at 550 °C with a heating rate of 5 °C min^{-1} in a muffle furnace for 3 h.[33]

2.2.2 Metal nanoparticle decoration. g-C_3N_4 (30 mg) was dispersed in 50 mL of deionized water (18.2 MΩ) and ultrasonicated for 30 min; then, 5 mg of $AgNO_3$ and 4 mL of methanol were added with ultrasonication for 10 min. The mixture was poured into a quartz photoreactor and continuously bubbled with argon, followed by irradiation with Hg light for 5 min, 30 min, 60 min, and 120 min; the achieved samples were denoted as CNAg-5, CNAg-30, CNAg-60, and CNAg-120, respectively. Similarly, Au and Pt nanoparticle-decorated g-C_3N_4 were prepared by modifying their metal precursors with Hg light for 30 min.

2.3 Characterization

The samples were characterized through X-ray diffraction (XRD, Bruker D8 Advance) using CuKα radiation (λ = 1.54178 Å). Transmission electron microscopy (TEM, JEOLJEM-2010) characterizations were performed at 200 kV. UV-vis diffuse reflectance spectra were performed on a UV-vis spectrophotometer (UV3600-MPC3100). Photoluminescence spectra were recorded on a spectrometer (OmniFluo990LSP) under an excitation wavelength of 310 nm at room temperature.

2.4 Photocatalytic reduction and analysis

Photocatalysis experiment was carried out in a container with a glass sleeve (0.2 L, Quartz). The light source was placed on top of the quartz reactor, and the outer layer was cooled with water. Potassium nitrate was used as a nitrate source for degradation. The initial concentration of nitrate (100 mg L^{-1}) was 10 times the maximum permissible concentration limit in drinking water. The catalyst concentration in the solution was 1.2 g L^{-1}, and methanol was used as a hole sacrificial agent. A 300 W xenon lamp (Microsolar 300) was used as the light source for the photocatalysis experiment. The solution was kept under constant stirring conditions during the whole experiment. After every 60 min, 1 mL of solution was extracted and filtered for ion chromatography measurements (Dionex Aquion and Dionex ICS-600).

The NO_3^- conversion rate ($C_{NO_3^-}$, %) and N_2 selectivity (S_{N_2}, %) were evaluated using eqn (1) and (2), respectively.

$$C(NO_3^-) = \frac{[NO_3^-]_0 - [NO_3^-]_t}{[NO_3^-]_0} \times 100\% \quad (1)$$

$$S(N_2) = \frac{[NO_3^-]_0 - [NO_3^-]_t - [NO_2^-]_t - [NH_4^+]_t}{[NO_3^-]_0 - [NO_3^-]_t} \times 100\% \quad (2)$$

where $[X]_0$ and $[X]_t$ are concentrations of various nitrogen species initially and at t time, respectively.

2.5 Electrochemical measurements

Firstly, the catalyst ink was obtained by dispersing 3 mg of catalyst in 90 μL of anhydrous ethanol and 10 μL of Nafion, followed by sonication for 10 min. Subsequently, 5 μL of the catalyst ink was coated on an L-shaped glassy carbon electrode and dried to obtain the working electrode. The Ag/AgCl electrode was used as the reference electrode and the Pt electrode as the counter electrode. The electrochemical impedance spectroscopy (EIS) results and Mott–Schottky curves of the catalysts were measured using an electrochemical workstation (CHENHUA, CHI660E, China) in 0.25 M K_2SO_4 solution. Cyclic voltammetry (CV) and linear scanning voltammetry (LSV) were performed in 0.25 M K_2SO_4 and 0.2 g per L KNO_3 solutions. For photoelectrochemical tests, a 300 W xenon lamp was used as the light source.

3. Results and discussion

The morphology of the achieved CNAg composite was determined using TEM (Fig. 1 and S1†). Under a longer

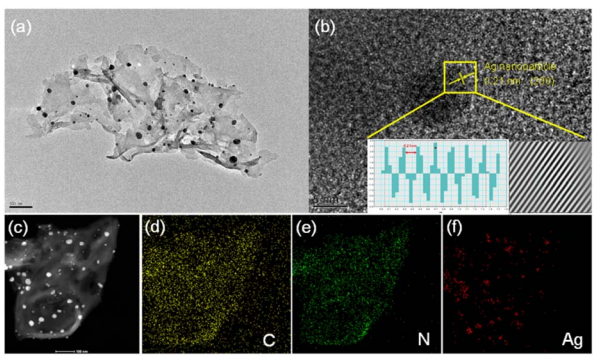

Fig. 1 (a) TEM image, (b) high-resolution image, and (c–f) EDS mapping of C, N and Ag elements of CNAg-30.

photodeposition duration, the size of Ag-NPs gradually increased (Fig. S2†). Fig. 1a shows the morphology of CNAg-30 under a photodeposition of 30 min; Ag-NPs of about 10 nm were loaded onto lamellar-structured g-C_3N_4. The lattice spacing of the exposed crystal faces of Ag-NPs was 0.21 nm, which was attributed to the (200) crystal faces, in accordance with the Fourier-transform image (Fig. 1b). Energy-dispersive X-ray maps (Fig. 1c–f) show the uniform distribution of C and N in g-C_3N_4 and the successful loading of Ag-NPs.

Fig. 2a shows the X-ray diffraction pattern of the as-prepared samples. The strong diffraction peak signal near 27.6° corresponds to the interlayer stacking planes of the conjugated heptazine frameworks.[34] After photodeposition of Ag for more than 30 min, the reduced Ag-NPs crystallized (PDF# 89-3722). Similar crystallization of Au-NPs is shown in Fig. S3.† Fig. 2b shows the light absorption of the as-prepared samples. The absorption peaks at 470 and 550 nm after loading Ag and Au nanoparticles were attributed to the localized surface plasmon resonance (LSPR) absorption of Ag- and Au-NPs, respectively. The forbidden bandgap of g-C_3N_4 was determined to be 2.8 eV from the Tauc plot (Fig. 2c) using the formula $(\alpha h\nu)^{1/n} = B(h\nu - E_g)$, where $n = 0.5$ since g-C_3N_4 is a direct bandgap semiconductor. The flat band potential of g-C_3N_4 was calculated to be −1.0 V (*vs.* SHE) based on the Mott–Schottky curve (Fig. 2d). Next, the conduction band edge of g-C_3N_4 was deduced to be −1.2 V (*vs.* SHE), according to the empirical formula that the semiconductor's conduction band value and flat-band potential differ by 0.2 eV,[35] which was consistent with previously reported results.[36]

Nitrate photocatalytic reduction performances were evaluated (Fig. 3a). Pure g-C_3N_4 showed no reduction effect. The CNAu composites showed no considerable photocatalytic reduction performance either. However, after loading Ag-NPs, the CNAg composites showed significant photocatalytic reduction efficiency toward nitrate. Especially, CNAg-30 exhibited the optimal nitrate reduction rate, and total nitrates were degraded within 1 h. Nevertheless, N_2 selectivity was only about 38% (Fig. 3b) and the predominant reduction product was NO_2^- (Fig. S4†), indicating that the reduction driving force was limited under xenon lamp irradiation, which contains limited UV light. The XRD patterns of the samples before and after the cyclic photocatalytic reaction were basically unchanged (Fig. S5†), indicating the relative stability of the as-prepared photocatalyst.

The photocatalytic mechanism of CNAg toward NO_3^- was revealed by comparing the photoelectrochemical response. A previous work claimed that the adsorbed hydrogen (H*) was the reason for the photocatalytic activity of CNAg.[37] However, if H* plays a role in NO_3^- reduction, the CNAu composite could reduce NO_3^- as it can produce H* too.[38] To reveal the function of H*, g-C_3N_4 decorated with Pt-NPs was synthesized (Fig. S6†). However, no nitrate reduction was observed in the CN–Pt system. Thus, H* should not be the real reason for the photocatalytic reduction of NO_3^-. Other possible mechanisms include specific surface catalytic activity, surface plasmonic hot electrons, or enhanced separation efficiency of photogenerated carriers. The CV curves of CNAg and CNAu in the dark with/

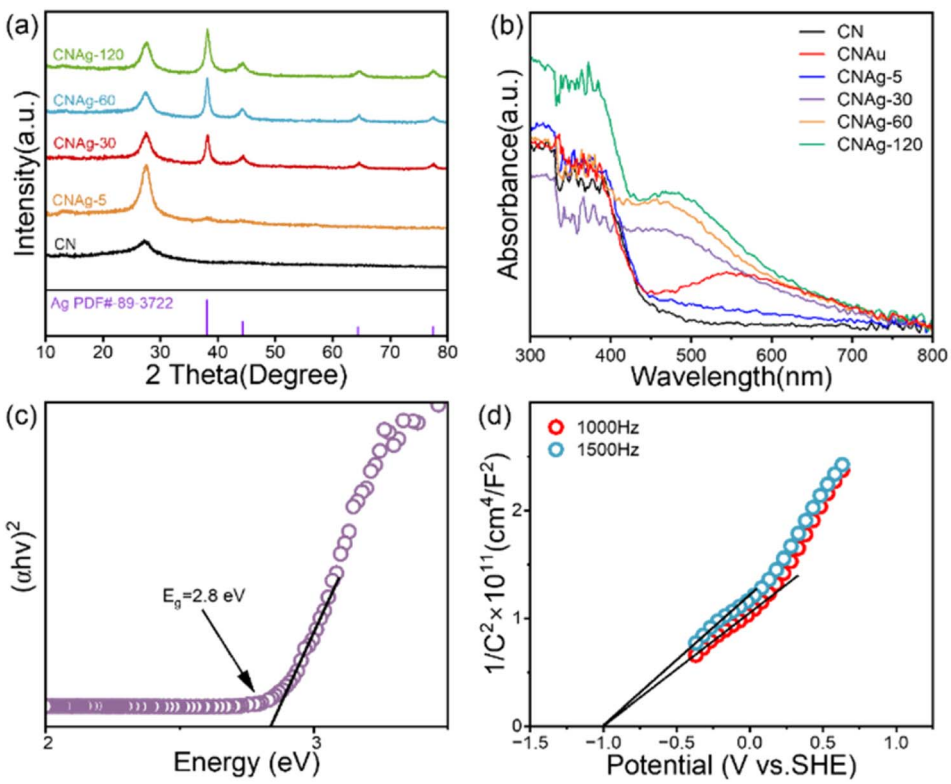

Fig. 2 (a) XRD and (b) UV-vis spectra of different samples. (c) Mott–Schottky and (d) Tauc plot of g-C_3N_4.

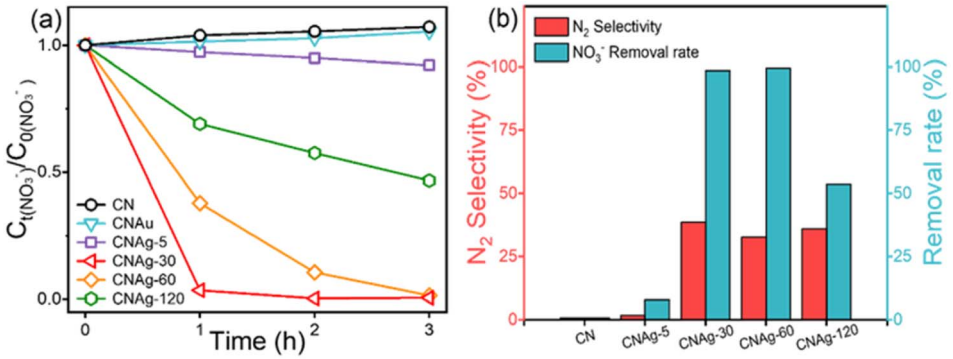

Fig. 3 (a) Nitrate removal dynamics of different samples and (b) removal rates and N_2 selectivity after 3 h of photocatalysis.

without NO_3^- illustrate that CNAu has no catalytic effect on NO_3^- (Fig. 4a); however, CNAg shows considerably increased catalytic activity with an onset potential of about −0.9 V (*vs.* Ag/AgCl). LSV curves for different light illumination conditions demonstrate that all the photocatalysts showed a light response (Fig. 4b), with the CNAg composite demonstrating the highest increase in current after light illumination, which is more clearly depicted in Fig. 4c. Under chopped light illumination, the photocurrent of CNAg was significantly higher than that of CNAu or bare g-C_3N_4. The slow response speed of the photocurrent demonstrated that the photocurrent is induced by the reduction of nitrate owing to the slow reaction dynamics. Additionally, the recombination probability of photogenerated carriers decreased after decoration with the metal nanoparticle, especially Ag-NPs, which was demonstrated by photoluminescence (PL) spectroscopy (Fig. 4d). Moreover, the surface photovoltage reveals that the CNAg composite can induce higher separation efficiency of photogenerated charge carriers (Fig. 4e), which can generate higher photocatalytic performance. Electrochemical impedance spectroscopy (Fig. S7†) reveals the CNAg composite has a lower impedance value, which is favourable for the separation and transport of charge carriers. Moreover, the zeta potentials (Fig. 4f) of CN and CNAu are negative, whereas they are positive for CNAg. As NO_3^- is negatively charged, electrostatic repulsion will inhibit the adsorption of NO_3^- for CN and CNAu, while CNAg can benefit adsorption, which can accelerate the photocatalytic reduction. Thus, based on the significant positive shift of the onset potential of NO_3^- reduction without light illumination (Fig. 4a) and no surface photovoltage at the wavelength of LSPR of the Ag- and Au-NPs (Fig. 4e), the surface catalytic activity of Ag-NPs, but not the plasmonic hot electrons, is believed to be the predominant reason for the outstanding photocatalytic NO_3^- reduction by CNAg. Furthermore, the Ag-NPs enhanced the separation efficiency of photogenerated electrons and holes, resulting in improved photocatalytic performance. Thus, the small size and large number of Ag nanoparticles should benefit the performance. Characterization results (Fig. 1, S1 and S2†) demonstrate that Ag nanoparticles with photodeposition of 30 min exhibited the optimal balance of size and density (*i.e.*,

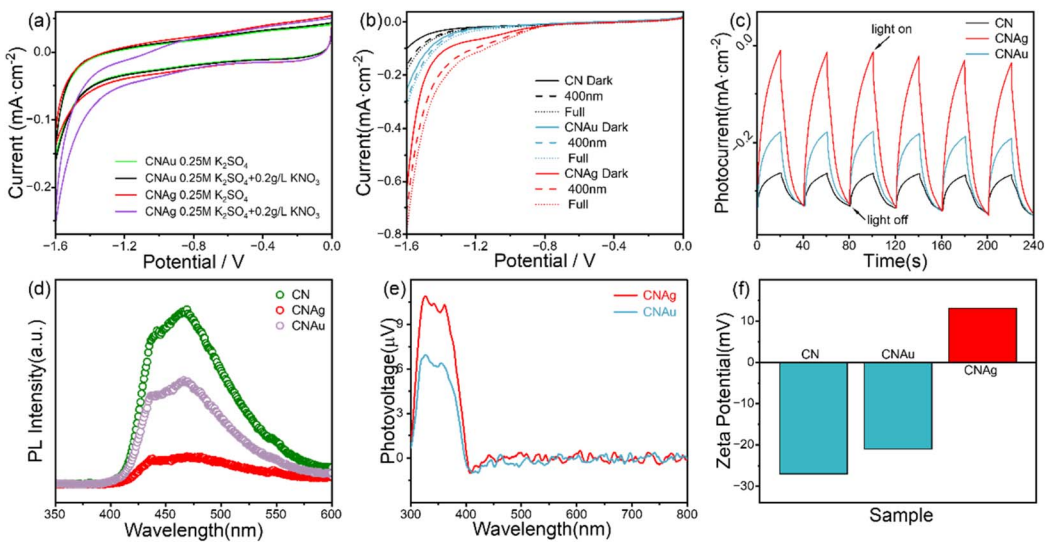

Fig. 4 (a) CV and (b) LSV curves of the CNAg, CNAu under different conditions. (c) Photocurrent responses with chopped light illumination. (d) PL curves, (e) surface photovoltage, and (f) zeta potential of the as-prepared photocatalysts.

small size and large density), which can provide more reaction sites that act as electron traps to accelerate the reduction reaction.

Dissolved O_2 has always existed in the real application case; however, the influence on photocatalytic nitrate reduction has not been studied. Fig. 5a depicts the ion chromatography measurement results recorded for a photocatalytic reaction of 6 h, in which the dissolved oxygen in the solution is not excluded in the initial 3 h and removed *via* argon bubbling in the next 3 h with CNAg-30 as a photocatalyst and methanol as a hole scavenger. When dissolved oxygen is present, a chromatography peak attributed to formic acid gradually increases with the photocatalytic duration, which is further confirmed by NMR hydrogen spectroscopy with a peak located near 8.15 ppm (Fig. 5b).[39–41] Although it has been widely reported that the oxidation of formic acid by holes can generate $^{\bullet}CO_2^-$ radicals, which can efficiently reduce NO_3^-,[42–45] the degradation of NO_3^- is not observed with dissolved O_2 based on the chromatography peak intensity of NO_3^- (Fig. 5a). This is probably attributed to the consumption of photogenerated electrons by reacting with dissolved O_2, producing superoxide radicals ($^{\bullet}O_2^-$), and the inverse oxidation of NO_2^- by the resultant hydroxyl radicals ($^{\bullet}OH$) or single-linear oxygen ($^1O_2$).[46,47] Argon bubbling was used to rapidly remove dissolved O_2. Thereafter, electrons and $^{\bullet}CO_2^-$ could efficiently reduce NO_3^-, resulting in a rapid reduction in concentration. If the photocatalysis is started in the absence of dissolved O_2, no considerable formic acid and the consequent $^{\bullet}CO_2^-$ can be produced, and thus, NO_3^- is reduced only by photogenerated electrons with limited driving force, which is determined by the conduction band of the photocatalyst. As a result, a large amount of NO_2^- (Fig. 5c, NO_2^- concentration is represented in blue and NO_3^- concentration in red) and low N_2 selectivity (Fig. 5d) are obtained. However, if the photocatalysis is carried out with dissolved O_2 for 3 h followed by subsequent removal of O_2, the reactivated photocatalytic reduction of NO_3^- produces no NO_2^- and extremely high N_2 selectivity (Fig. 5d) as a result of the supplementary reduction capacity of $^{\bullet}CO_2^-$ radicals generated from formic acid. Thus, the dissolved O_2 demonstrates a critical inhibition of photocatalytic reduction of NO_3^-, although it can help produce $^{\bullet}CO_2^-$ to improve the catalytic activity and N_2 selectivity. As a result, in future research, the design of a photocatalyst or device without influence of dissolved O_2 would be the biggest bottleneck in practical applications.

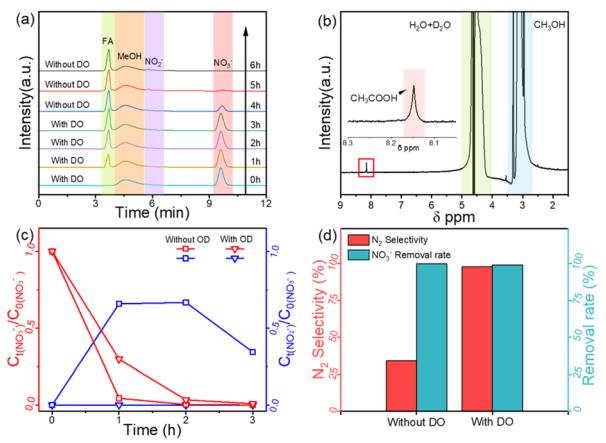

Fig. 5 (a) Ion chromatogram of photocatalysis with and without dissolved O_2. (b) ^1H NMR spectroscopy of photocatalytic production with dissolved O_2. (c) Evolution of NO_3^- and NO_2^- during photocatalysis with and without dissolved O_2 and (d) NO_3^- removal rate and N_2 selectivity after 3 h.

4. Conclusions

In summary, Ag- and Au-NPs were *in situ* grown on g-C_3N_4 for nitrate reduction. Ag-NPs showed improved surface catalytic activity and carrier separation efficiency, which significantly enhanced photocatalytic NO_3^- reduction. Additionally, CNAg could oxidize methanol to formic acid and, consequently, to $^{\bullet}CO_2^-$ radicals in the dissolved O_2 atmosphere, which could improve the reduction dynamics and N_2 selectivity. However, the dissolved O_2 in practical cases would be a critical bottleneck owing to the consumption of photogenerated electrons. The work provides new perspectives for subsequent development of solar-driven removal of nitrate from contaminated water.

Data availability

All the data related to this work are available in the main manuscript or ESI.†

Conflicts of interest

There are no conflicts to declare.

Acknowledgements

This work was supported by the National Natural Science Foundation of China (Grants No. 52472309, 52232007, 51972308) and HFIPS Director's Fund (Grant No. BJPY2022B03).

References

1 J. Wang, X. Liu, A. H. W. Beusen and J. J. Middelburg, *Environ. Sci. Technol.*, 2023, **57**, 19395–19406.
2 S. Qu, L. Duan, Z. Shi, H. Mao, G. Wang, T. Liu, R. Yu and X. Peng, *J. Cleaner Prod.*, 2022, **376**, 134289.
3 J. Yan, J. Chen and W. Zhang, *Water Res.*, 2023, **243**, 120379.
4 P. J. Clemmensen, J. Schullehner, N. Brix, T. Sigsgaard, L. T. Stayner, H. A. Kolstad and C. H. Ramlau-Hansen, *Curr. Environ. Health Rep.*, 2023, **10**, 250–263.
5 N. G. Hord, *Curr. Atheroscler. Rep.*, 2011, **13**, 484–492.
6 N. Medgyesi Danielle, B. Trabert, J. Sampson, J. Weyer Peter, A. Prizment, A. Fisher Jared, E. Beane Freeman Laura, H. Ward Mary and R. Jones Rena, *Environ. Health Perspect.*, 2022, **130**, 057012.
7 J. A. Alcolea, C. Donat-Vargas, A. C. Chatziioannou, P. Keski-Rahkonen, N. Robinot, A. J. Molina, P. Amiano, I. Gómez-Acebo, G. Castaño-Vinyals, L. Maitre, M. Chadeau-Hyam, S. Dagnino, S. L. Cheng, A. Scalbert, P. Vineis,

M. Kogevinas and C. M. Villanueva, *Environ. Sci. Technol.*, 2023, **57**, 19316–19329.
8 S. Lu, Q. Zhu and R. Li, *J. Colloid Interface Sci.*, 2023, **652**, 1481–1493.
9 P. Loganathan, S. Vigneswaran and J. Kandasamy, *J. Environ. Manage.*, 2013, **131**, 363–374.
10 B. Yan, K. Kato, S. Shimoda, R. Otomo and Y. Kamiya, *Chem. Eng. J.*, 2024, **498**, 155721.
11 T. Nur, W. G. Shim, P. Loganathan, S. Vigneswaran and J. Kandasamy, *Int. J. Environ. Sci. Technol.*, 2014, **12**, 1311–1320.
12 J. Ma, W. Wei, G. Qin, L. Jiang, N. Hing Wong, J. Sunarso and S. Liu, *Sep. Purif. Technol.*, 2022, **292**, 121010.
13 Y. Zhou, L. Zhang, Z. Zhu, M. Wang, N. Li, T. Qian, C. Yan and J. Lu, *Angew. Chem., Int. Ed.*, 2024, **63**, e202319029.
14 J. Bi, C. Peng, H. Xu and A.-S. Ahmed, *Desalin. Water Treat.*, 2011, **34**, 394–401.
15 H. Duan, L. Zhang, H. Wang, S. Li, X. Li and Y. Zhuang, *Sci. Total Environ.*, 2024, **951**, 175745.
16 Z. S. Wei, J. B. Wang, Z. S. Huang, X. L. Xiao, M. R. Tang, B. L. Li and X. Zhang, *Biomass Bioenergy*, 2019, **126**, 34–40.
17 A. Fujishima and K. Honda, *Nature*, 1972, **238**, 37–38.
18 F. Yang, P. Hu, F. Yang, X.-J. Hua, B. Chen, L. Gao and K.-S. Wang, *Tungsten*, 2023, **6**, 77–113.
19 H. O. Tugaoen, S. Garcia-Segura, K. Hristovski and P. Westerhoff, *Sci. Total Environ.*, 2017, **599–600**, 1524–1551.
20 J. M. A. Freire, M. A. F. Matos, D. S. Abreu, H. Becker, I. C. N. Diógenes, A. Valentini and E. Longhinotti, *J. Environ. Chem. Eng.*, 2020, **8**, 103844.
21 W. Yang, J. Wang, R. Chen, L. Xiao, S. Shen, J. Li and F. Dong, *J. Mater. Chem. A*, 2022, **10**, 17357–17376.
22 S. Yu, S. Shen, C. Zhang, R. Chen, H. Dan, J. Li and F. Dong, *Appl. Catal., B*, 2024, **358**, 124419.
23 W.-M. Wang, S.-J. Tseng, Y.-S. Huang, Q.-Y. Wu, W.-L. Wang and J. J. Wu, *J. Ind. Eng. Chem.*, 2023, **119**, 386–394.
24 K. T. Ranjit, R. Krishnamoorthy and B. Viswanathan, *J. Photochem. Photobiol., A*, 1994, **81**, 55–58.
25 G. Liu, S. You, M. Ma, H. Huang and N. Ren, *Environ. Sci. Technol.*, 2016, **50**, 11218–11225.
26 Z. Hou, F. Chen, J. Wang, C. P. François-Xavier and T. Wintgens, *Appl. Catal., B*, 2018, **232**, 124–134.
27 H. Shi, C. Li, L. Wang, W. Wang, J. Bian and X. Meng, *Sep. Purif. Technol.*, 2022, **300**, 121854.
28 R. Yin, P. U. Dao, J. Zhao, K. Wang, S. Lu, C. Shang and H. Ren, *Environ. Sci. Technol.*, 2024, **58**, 20676–20686.
29 K. Yin, Z. Yan, N. Fang, W. Yu, Y. Chu, S. Shu and M. Xu, *Sep. Purif. Technol.*, 2023, **325**, 124636.
30 H. Wang, X. Li, X. Zhao, C. Li, X. Song, P. Zhang, P. Huo and X. Li, *Chin. J. Catal.*, 2022, **43**, 178–214.
31 C. Wang, S. Dong, Y. Wang, T. Guo, G. Gao, Z. Lu and B. Pan, *Chem. Eng. J.*, 2020, **397**, 125435.
32 Y. Kim, E. B. Creel, E. R. Corson, B. D. McCloskey, J. J. Urban and R. Kostecki, *Adv. Energy Mater.*, 2018, **8**, 1800363.
33 P. M. Schaber, J. Colson, S. Higgins, D. Thielen, B. Anspach and J. Brauer, *Thermochim. Acta*, 2004, **424**, 131–142.
34 A. Zambon, J. M. Mouesca, C. Gheorghiu, P. A. Bayle, J. Pecaut, M. Claeys-Bruno, S. Gambarelli and L. Dubois, *Chem. Sci.*, 2016, **7**, 945–950.
35 F. Li, X. Li, S. Tong, J. Wu, T. Zhou, Y. Liu and J. Zhang, *Nano Energy*, 2023, **117**, 108849.
36 N. Shehzad, M. Tahir, K. Johari, T. Murugesan and M. Hussain, *J. CO_2 Util.*, 2018, **26**, 98–122.
37 S. J. P. Varapragasam, J. M. Andriolo, J. L. Skinner and E. M. Grumstrup, *ACS Omega*, 2021, **6**, 34850–34856.
38 Z. Mo, H. Xu, Z. Chen, X. She, Y. Song, P. Yan, Y. Xu, Y. Lei, S. Yuan and H. Li, *Chin. J. Catal.*, 2018, **39**, 760–770.
39 W.-M. Zhang, K.-W. Feng, R.-G. Hu, Y.-J. Guo and Y. Li, *Chem*, 2023, **9**, 430–442.
40 J. Shi, H. He, S. Zhou, J. Li and W. Cai, *Green Chem.*, 2024, **26**, 2638–2644.
41 J. Wu, J. Wen and Y.-X. Yu, *Appl. Surf. Sci.*, 2021, **565**, 150567.
42 L. Wang, W. Fu, Y. Zhuge, J. Wang, F. Yao, W. Zhong and X. Ge, *Chemosphere*, 2021, **278**, 130298.
43 H. Shi, C. Li, R. Zheng, L. Wang, W. Wang, J. Bian and X. Meng, *J. Cleaner Prod.*, 2023, **407**, 137088.
44 H. Shi, C. Li, L. Wang, W. Wang and X. Meng, *J. Hazard. Mater.*, 2022, **424**, 127711.
45 I. Hong, H. S. Moon, B. J. Park, Y.-A. Chen, Y.-P. Chang, B. Song, D. Lee, Y. Yun, Y.-J. Hsu, J. W. Han and K. Yong, *Chem. Eng. J.*, 2024, **484**, 149506.
46 K. Tennakone, S. Punchihewa and R. U. Tantrigoda, *Environ. Pollut.*, 1989, **57**, 299–305.
47 L. Yang, Z. Chen, Q. Cao, H. Liao, J. Gao, L. Zhang, W. Wei, H. Li and J. Lu, *Adv. Mater.*, 2024, **36**, 2306758.